Intermolecular, Inc. - Award DE- EE0007213
Final scientific/technical report – December 2017

Federal Agency:	**Department of Energy**
FOA Name and #:	**FY 2015 VTO Incubator, DE-FOA-0001213**
Report Type:	**Final Scientific/Technical Report**
Award #:	**DE-EE0007213**
Award Type:	**Cooperative Agreement**
Prime Recipient:	**Intermolecular, Inc 3011 N 1st St San Jose, CA 95134 jeroen.vanduren@intermolecular.com (408) 582-5577**
Prime Recipient Type:	**Private Company**
Project Title:	**HIGH-THROUGHPUT COMBINATORIAL DEVELOPMENT OF HIGH-ENTROPY ALLOYS FOR LIGHT-WEIGHT STRUCTURAL APPLICATIONS**
Principal Investigator:	**Dr. Jeroen van Duren Director, Intermolecular, Inc jeroen.vanduren@intermolecular.com (408) 582-5577**
Teaming members	**Prof. Koch, North Carolina State University Prof. Luo, Ohio State University Dr. Sample, Arconic Dr. Sachdev, General Motors**
Prime Recipient's DUNS:	**362192473**
Date of Report:	**December, 2017**
Reporting Period:	**Oct 1, 2015 – Sept 30, 2017**
Project Period:	**Oct 1, 2015 – Sept 30, 2017**
Report Frequency:	**At project closeout**

Disclaimer

Contents

1 Executive Summary

The primary limitation of today's lightweight structural alloys is that specific yield strengths (SYS) higher than 200MPa x cc/g (typical value for titanium alloys) are extremely difficult to achieve. This holds true especially at a cost lower than 5$/kg (typical value for magnesium alloys). Recently, high-entropy alloys (HEA) have shown promising SYS, yet the large composition space of HEA makes screening compositions complex and time-consuming.

Over the course of this 2-year project we started from 150 billion compositions and reduced the number of potential low-density (<5g/cc), low-cost (<5$/kg) high-entropy alloy (LDHEA) candidates that are single-phase, disordered, solid-solution (SPSS) to a few thousand compositions. This was accomplished by means of machine learning to guide design for SPSS LDHEA based on a combination of recursive partitioning, an extensive, experimental HEA database compiled from 24 literature sources, and 91 calculated parameters serving as phenomenological selection rules.

Machine learning shows an accuracy of 82% in identifying which compositions of a separate, smaller, experimental HEA database are SPSS HEA. Calculation of Phase Diagrams (CALPHAD) shows an accuracy of 71-77% for the alloys supported by the CALPHAD database, where 30% of the compiled HEA database is not supported by CALPHAD. In addition to machine learning, and CALPHAD, a third tool was developed to aid design of SPSS LDHEA. Phase diagrams were calculated by constructing the Gibbs-free energy convex hull based on easily accessible enthalpy and entropy terms. Surprisingly, accuracy was 78%.

Pursuing these LDHEA candidates by high-throughput experimental methods resulted in SPSS LDHEA composed of transition metals (e.g. Cr, Mn, Fe, Ni, Cu) alloyed with Al, yet the high concentration of Al, necessary to bring the mass density below 5.0g/cc, makes these materials hard and brittle, body-centered-cubic (BCC) alloys. A related, yet multi-phase BCC alloy, based on Al-Cr-Fe-Ni, shows compressive strain >10% and specific compressive yield strength of 229 MPa x cc/g, yet does not show ductility in tensile tests due to cleavage. When replacing Cr in Al-Cr-Fe-based 4- and 5-element LDHEA with Mn, hardness drops 2x. Combined with compression test results, including those on the ternaries Al-Cr-Fe and Al-Mn-Fe suggest that Al-Mn-Fe-based LDHEA are still worth pursuing. These initial results only represent one compressive stress-strain curve per composition without any property optimization. As such, reproducibility needs to be followed by optimization to show their full potential.

When including Li, Mg, and Zn, single-phase Li-Mg-Al-Ti-Zn LDHEA has been found with a specific ultimate compressive strength of 289MPa x cc/g. Al-Ti-Mn-Zn showed a specific ultimate compressive strength of 73MPa x cc/g. These initial results after hot isostatic pressing (HIP) of the ball-milled powders represent the lower end of what is possible, since no secondary processing (e.g. extrusion) has been performed to optimize strength and ductility.

Compositions for multi-phase (e.g. dual-phase) LDHEA were identified largely by automated searches through CALPHAD databases, while screening for large face-centered-cubic (FCC) volume fractions,

followed by experimental verification. This resulted in several new alloys. Li-Mg-Al-Mn-Fe and Mg-Mn-Fe-Co ball-milled powders upon HIP show specific ultimate compressive strengths of 198MPa x cc/g and 45MPa x cc/g, respectively. Several malleable quarternary Al-Zn-based alloys have been found upon arc/induction melting, yet with limited specific compressive yield strength (<75 MPa x cc/g). These initial results are all without any optimization for strength and/or ductility.

High-throughput experimentation allowed us to triple the existing experimental HEA database as published in the past 10 years in less than 2 years which happened at a rate 10x higher than previous methods. Furthermore, we showed that high-throughput thin-film combinatorial methods can be used to get insight in isothermal phase diagram slices.

Although it is straightforward to map hardness as a function of composition for sputtered, thin-film, compositional gradients by nano-indentation and compare the results to micro-indentation on bulk samples, the simultaneous impact of composition, roughness, film density, and microstructure on hardness requires monitoring all these properties as a function of location on the compositional gradient, including dissecting the impact of these 4 factors on the hardness map. These additional efforts impact throughput significantly.

This work shows that a lot of progress has been made over the years in predicting phase formation that aids the discovery of new alloys, yet that a lot of work needs to be done to predict phases more accurately for LDHEA, whether done by CALPHAD or by other means. More importantly, more work needs to be done to predict mechanical properties of novel alloys, like yield strength, and ductility. Furthermore, this work shows that there is a need for the generation of an empirical alloy database covering strategic points in a multi-dimensional composition space to allow for faster and more accurate predictive interpolations to identify the oasis in the dessert more quickly. Finally, this work suggests that it is worth pursuing a ductile alloy with a SYS > 300 MPa x cc/g in a mass density range of 6-7 g/cc, since the chances for a single-phase or majority-phase FCC increase significantly. Today's lightweight steels are in this density range.

2 Original Hypotheses

The primary limitation of today's lightweight structural alloys is that specific yield strengths (SYS) higher than 200MPa x cc/g (typical value for titanium alloys) are extremely difficult to achieve. This holds true especially at a cost lower than 5$/kg (typical value for magnesium alloys). Recently, high-entropy alloys (HEA) have shown promising SYS, yet the large composition space of HEA makes screening compositions complex and time-consuming.

HEAs are a new class of multi-principal element alloys, a field over a decade old, in which the design of the alloys is based not on adding solutes at low weight-% to a single "base" element, but rather on choosing multiple elements all around equi-atomic concentrations. Several definitions for HEA exist, typically based on composition, or configurational entropy, and sometimes with the motivation to produce a single-phase, disordered, solid solution (SPSS).

HEA have potential applications outside light-weighting which includes protective coatings, catalysts, high-temperature environments, magnetics (e.g. rare-earth replacement), and a range of other areas that require extraordinary material properties or cost reduction. As such, HEA open up a wealth of new opportunities for the US economy.

LDHEAs (e.g. Li-Mg-Al-Sc-Ti (1)) have been shown to possess higher SYS than traditional alloys. In addition, because each element in the LDHEA is at a high atomic-%, it is possible to tailor macroscopic functional characteristics in a way not previously explored for traditional base alloys. As such, LDHEAs have the potential to combine a dramatically improved SYS with a concomitant improvement in the balance between strength and ductility of metals, together with a reduced sensitivity to minority elements, and corrosion.

Preliminary LDHEA studies (1) have demonstrated SYS of 749 MPa x cc/g (see Table 1), with the potential to reduce primary metal weight in automotive applications by almost 50% (2), assuming a blend of stiffness and strength limited metal parts. This does not include downsizing (engine, brakes, cooling system) made possible by primary metal light-weighting. Such materials could be highly impactful in DOE's effort toward light-weighting, and are an ideal candidate for future MYPPs.

Each of the key elements of our proposed approach are commonly used for other, related applications. The accumulated experimental work on HEA over the past decade (3-5) has made it possible to improve the predictions on phase formation and hardness for LDHEA through phenomenological selection rules, as evidenced by Koch's LDHEA work (1). These empirical selection rules are a refinement to the Hume-Rothery rules, made specifically for HEA. Similarly, CALPHAD modeling of various alloys has been extensively validated, including more recently modeling of HEA (6). Traditional thin-film alloy development has been demonstrated through multiple studies as a good screening tool for bulk alloys (7).

Table 1. SOTA lightweight structural alloys, plus Program Targets

						Yr 1 Target	Yr 2 Target
Material	AHSS	Ti-alloy	Mg-alloy	Al-alloy	SOTA LDHEA	Non-Sc LDHEA	Non-Sc LDHEA
Yield Strength (MPa)	1000	880	285	230	2000	1500	3000
Mass density (gram/cm^3)	7.85	4.43	1.80	2.70	2.67	5.00	5.00
SYS (MPa x cm^3/gram)	127	199	158	85	749	300	600
Cost ($/kg)	$1.50/kg	$20/kg	$5/kg	$2.75/kg	$5,000/kg	$5/kg	$5/kg
Performance Cost Index	0.58	4.69	0.84	0.77	469	1.01	0.72

3 Approach

3.1 High-throughput material design and experimentation

The approach taken to accelerate the discovery of a promising LDHEA is based on a combination of high-throughput material design, prediction validation by fabricating a single composition via a small bulk fabrication method, subsequent mapping of the composition space by thin-film sputter (PVD) deposition and annealing, followed by taking the most promising compositions to a larger bulk scale fabrication and thermo-mechanical optimization, see Figure 1 below.

The material design is accelerated by database-driven design. Multiple approaches are used in parallel to ensure a well-balanced approach. In addition to phenomenological selection rules, experimental phase diagrams, CALPHAD, and a simple phase diagram tool is used. A brief overview of pros and cons is given below in Table 2.

Item	PSR	CALPHAD	SPD
Designed for experimentally unassessed systems	yes	no	yes
Results potentially biased towards database input	yes	yes	no
fcc/bcc/hcp aware	possible	yes	no
Temperature aware	possible	yes	yes
Distinguishes single-phase from two-phase disordered solid solution mixtures	no	yes	no
Adjustable for new experimental data	yes	difficult	no
Basis	Experiment	Experiment + Thermodynamics	Model + DFT + Thermodynamics

Table 2. Comparison of phenomenological selection rules (PSR), CALPHAD, and simple phase diagrams (SPD) for the purpose of material design of LDHEA.

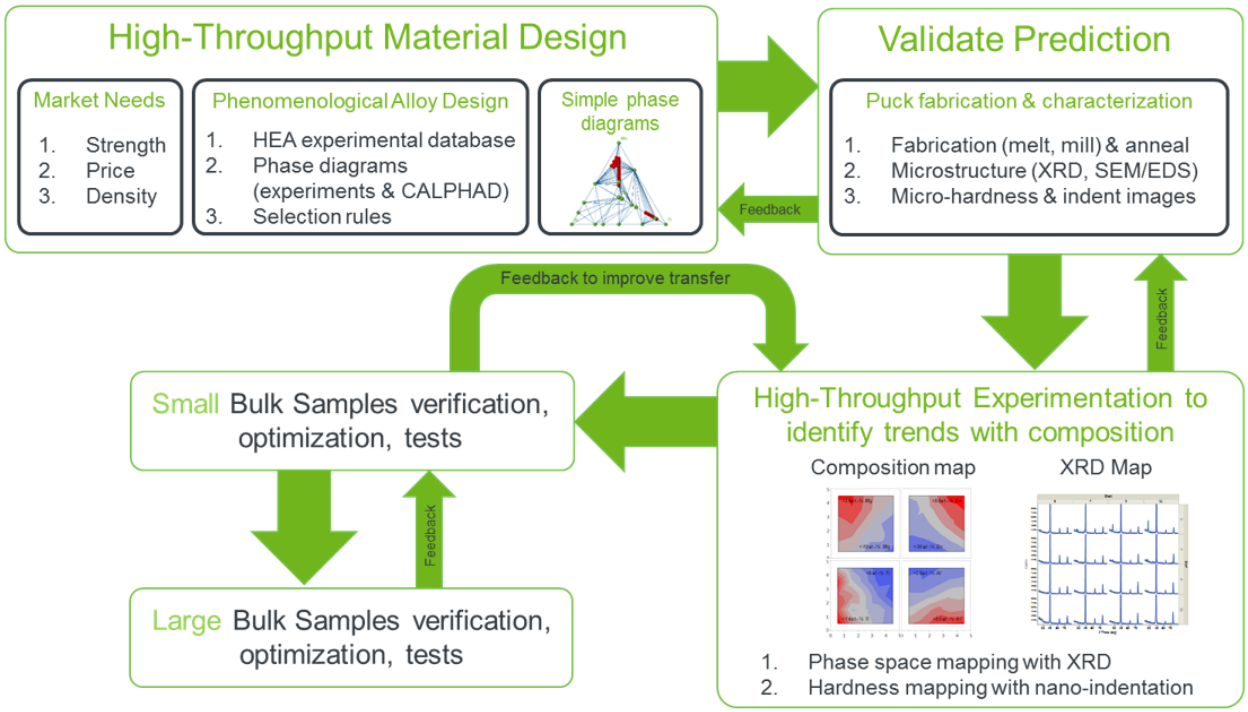

Figure 1. Visualization of the high-throughput material design and experimentation approach.

3.2 High-throughput material design

3.2.1 Databases used for high-throughput material design

High-throughput material design relies heavily on databases. Five input tables were created to allow for high-throughput material design. In addition, TCAL4, TCNI8, and TCHEA1 were used within the Thermo-Calc CALPHAD software package. Regarding the 5 input tables. The first table contains 20 parameters per element for 48 elements of the periodic table, collected from multiple sources. Table 3 shows an overview on parameters used for the elements.

ID	Table Header	Description
1	Atomic # of Elements	Atomic number of element
2	Symbol	Symbol of element
3	Element	Element
4	VEC	Valence electron concentration
5	sap	Sum of s and p electrons for Friedel model, see Acta Materialia 75 (2014) 297–306
6	Atomic Mass (gr/mole)	Atomic mass in gram/mole
7	Melting Point (C)	Melting point in Celsius
8	Mass Density (g/cm3)	Mass density in gram/cc
9	Molar volume (cm3/mole)	Molar volume in cc/mole
10	Allen Electronegativity	Electronegativity based on Allen scale, see J. Am. Chem. Soc. 2000, 122, 5132-5137
11	Pauling Electronegativity	Electronegativity based on Pauling scale
12	AR Electronegativity	Electronegativity based on Allred-Rochow scale, see J. Am. Chem. Soc. 2000, 122, 5132-5137
13	Wiki-E. At. R. (pm)	Atomic radius (in pm) from Wikipedia
14	MEH At. R. (pm)	Atomic radius (in pm) from Materials Science and Engineering Handbook (CRC, 3rd edition)
15	GUO At. R. (pm)	Atomic radius (in pm) from GUO, Progress in Natural Science: Materials International 21(2011) 433-446
16	Zhang At. R. (pm)	Atomic radius (in pm) from Zhang, Progress in Materials Science 61 (2014) 1-93
17	CN12 At. R. (pm)	Atomic radius for CN = 12 (in pm) from W.B. Pearson's (after Teatum, Gschneidner, and Waber)
18	MEH Ion. R. (pm)	Ionic radius (in pm) from Materials Science and Engineering Handbook (CRC, 3rd edition)
19	Price ($/kg)	Raw metal price in $/kg for early 2015 based on multi-year trends, not spot prices
20	Young's Modulus (GPa)	Young's Modulus in GPa
21	Shear Modulus (GPa)	Shear Modulus in GPa
22	Compressibility (1/GPa)	Compressibility in 1/GPa
23	Crystal Structure	Most common crystal structure

Table 3. Parameters tabulated per element of the periodic table for each of the 48 elements investigated.

An overview of the 48 elements of the periodic table investigated, including values for 5 out of 20 parameters for each element, is shown in Table 4.

Atomic # of Elements	Symbol	Element	VEC	Mass Density (g/cm3)	Pauling Electronegativity	MEH At. R. (pm)	Price ($/kg)
3	Li	Lithium	1	0.53	0.98	152	75
4	Be	Beryllium	2	1.85	1.57	114	240
5	B	Boron	3	2.34	2.04	97	50
6	C	Carbon	4	2.26	2.55	77	1
11	Na	Sodium	1	0.97	0.93	186	5
12	Mg	Magnesium	2	1.74	1.31	160	3
13	Al	Aluminum	3	2.70	1.61	143	3
14	Si	Silicon	4	2.33	1.90	117	3
19	K	Potassium	1	0.86	0.82	231	25
20	Ca	Calcium	2	1.55	1.00	197	5
21	Sc	Scandium	3	2.99	1.36	160	18,000
22	Ti	Titanium	4	4.51	1.54	147	15
23	V	Vanadium	5	6.11	1.63	132	75
24	Cr	Chromium	6	7.19	1.66	125	10
25	Mn	Manganese	7	7.47	1.55	112	3
26	Fe	Iron	8	7.87	1.83	124	1
27	Co	Cobalt	9	8.92	1.88	125	30
28	Ni	Nickel	10	8.91	1.91	125	15
29	Cu	Copper	11	8.93	1.90	128	5
30	Zn	Zinc	12	7.14	1.65	133	3
31	Ga	Gallium	3	5.91	1.81	135	600
32	Ge	Germanium	4	5.32	2.01	122	1,250
33	As	Arsenic	5	5.78	2.18	125	2
37	Rb	Rubidium	1	1.53	0.82	251	25,000
38	Sr	Strontium	2	2.64	0.95	215	1,000
39	Y	Yttrium	3	4.47	1.22	181	80
40	Zr	Zirconium	4	6.51	1.33	158	100
41	Nb	Niobium	5	8.57	1.60	143	200
42	Mo	Molybdenum	6	10.22	2.16	136	30
47	Ag	Silver	11	10.50	1.93	144	560
48	Cd	Cadmium	12	8.65	1.69	150	3
49	In	Indium	3	7.31	1.78	157	720
50	Sn	Tin	4	7.27	1.96	158	25
51	Sb	Antimony	5	6.69	2.05	161	2
56	Ba	Barium	2	3.59	0.89	217	50
57	La	Lanthanum	3	6.17	1.10	187	5
58	Ce	Cerium	3	6.71	1.12	182	5
59	Pr	Praseodymium	3	6.77	1.13	183	100
60	Nd	Neodymium	3	7.00	1.14	182	85
62	Sm	Samarium	3	7.54	1.17	181	20
64	Gd	Gadolinium	3	7.89	1.20	180	40
66	Dy	Dysprosium	3	8.56	1.22	177	350
67	Ho	Holmium	3	8.78	1.23	176	1,000
72	Hf	Hafnium	4	13.31	1.30	159	500
73	Ta	Tantalum	5	16.67	1.50	147	150
74	W	Tungsten	6	19.30	2.36	137	100
82	Pb	Lead	4	11.34	2.33	175	3
83	Bi	Bismuth	5	9.79	2.02	182	17

Table 4. An overview of the 48 elements of the periodic table investigated for LDHEA design, including 5 parameters out of 20 parameters for each element. For explanation of column headers, see Table 3.

The second table involves a matrix of the enthalpy of mixing of the binary liquid in an A-B system at an equi-atomic composition based on Miedema's model and taken from literature (8). The third table involves a matrix of the enthalpy of mixing (solution) of the binary liquid at infinite dilution for A in B in an A-B system based on Miedema's model, taken from literature (9). The fourth table provides a matrix of Density-Functional-Theory-calculated enthalpy of formation terms of the lowest energy structure of each binary compound, taken from literature (10) and the Materials Project (https://materialsproject.org/).

An experimental HEA database was compiled from 24 literature sources (see Table 5) listing whether HEA compositions resulted in single-phase, disordered, solid solutions (SPSS, e.g. FCC, BCC, or HCP), or multiple phases. The database contains 1,490 entries, and all process conditions are being considered

(whether ball milled, sputtered, as-cast, annealed, etc.). After removing duplicates and (perceived) conflicts >550 entries are left. Most entries have a mass density in the 7-8g/cc and are heavily concentrated around the typical 3d transition metal HEA (11). The experimental HEA database contains only a few data points with density <5g/cc, most of which are not SPSS. The data points that are SPSS with a density <5g/cc are the result of ball milling.

Resources HEA Database
Acta Materialia, 104 (2016) 172-179
Acta Materialia, 75 (2014) 297–306
CALPHAD, 50 (2015) 32–48
Entropy, 2013, 15, 5338-5345
High-Entropy Alloys, Elsevier, 2014, [Murty, Yeh, Ranganathan]
Intermetallics, 41 (2013) 96-103
Intermetallics, 58 (2015) 1-6
Intermetallics, 59 (2015) 75-80
International Journal of Minerals, Metallurgy, and Materials, 2016, 23 (1), pp 77-82
JOM, Vol. 66, No. 10, 2014, p. 2009
JOM, Vol. 66, No. 10, 2014, p. 2021
Journal of Alloys and Compounds, 460 (2008) 253–257
Journal of Alloys and Compounds, 506 (2010) 210–215
Journal of Alloys and Compounds, 658 (2016) 603-607
Materials Research Letters, Volume 3, 2015 - Issue 2, Pages 95-99
Mater. Sci. Forum, 686 (2011) 235
Materials Characterization, 110 (2015) 116–125
Materials Chemistry and Physics, 132 (2012) 233-238
Materials Letters, 169 (2016) 62-64
Materials Science and Technology, 31(15), 2015, Pages 1842-1849
Nature Communications 6, Article number: 6529 (2015)
Progress in Natural Science: Materials Inter., 21 (2011), p. 433-446
Progress in Natural Science: Materials Inter., 24 (4), 2014, p. 305–312
Koch, North Carolina State University, unpublished

Table 5. Main literature sources to construct the experimental HEA database.

3.2.2 Computations for high-throughput material design

Computations are required to implement fast filtering of billions of compositions (LDHEA design) based on phenomenological selection rules (“cut-off” values), machine learning, construction of a simple phase diagram, and CALPHAD.

The computational part for both the phenomenological selection rules and machine learning was implemented in BIOVIA Pipeline Pilot version 9.2, a scientific software platform that includes a wide variety of functionality for data analytics and modeling (see http://accelrys.com). The main method for the machine learning was Recursive Partitioning, a method that constructs decision trees to classify data based on a set of input and output variables (also referred to as Classification and Regression Trees, CART).

In addition to the use of phenomenological selection rules and machine learning, we calculate a simple phase diagram by constructing the Gibbs-free energy convex hull using Pipeline Pilot with qhull. Formation enthalpies for ordered compounds are based on DFT calculations (https://materialsproject.org/) without entropy terms. Only fully ordered compounds are being considered, no ordered compounds with fractional occupancies are included. Disordered solid solutions

are modeled based on either binary equi-atomic Miedema enthalpy terms (3), or the sum of chemical and elastic enthalpy terms (12) with either ideal or the sum of ideal and excess configurational entropy (13) terms.

CALPHAD computations are made via the software package of Thermo-Calc.

3.2.3 Parameters for phenomenological selection rules and machine learning

The parameters calculated per LDHEA composition in Pipeline Pilot include thermodynamic, geometric, electronic and physical parameters, see Table 6. Typical phenomenological selection rule parameters are used (up to calendar year 2016), yet often calculated based on multiple sources, like several electronegativity scales, and several sources for atomic size. This will allow a detailed comparison of the predictability of the different parameters based on different sources.

Furthermore, the Gibbs-free energy is calculated at various temperatures (e.g. 300K, 600K, and 1200K) based on the most commonly used enthalpy terms in the HEA community (8), and less commonly used enthalpy terms in the HEA community (12). The latter being the sum of chemical and elastic enthalpy contributions, instead of the binary equi-atomic Miedema enthalpy terms (3). In addition, the sum of ideal and excess configurational entropy (13) is used in the Gibbs-free energy calculations, as comparison with the purely ideal configurational entropy term.

A recent, further expansion on enthalpy terms (not applied in this work) applied to HEA can be found in literature (14). Some more recent phenomenological selection rule parameters (2016 and beyond) are not included, like ϕ and λ (15).

ID	Table Header	Description	Literature Source for equation
1	Formula	Alloy composition as entered	n/a
2	Formula_pc	Alloy composition in at.-%	n/a
3	Price	Alloy metal price based on rule of mixtures	Nature Communications 6, Article number: 6529 (2015)
4	Density	Alloy mass density based on rule of mixtures	Nature Communications 6, Article number: 6529 (2015)
5	Ave_Melting_Point	Alloy melting temperature based on rule of mixtures	Materials Chemistry and Physics, 132 (2012) 233-238
6	Youngs_Modulus	Young's modulus based on rule of mixtures	Nature Communications 6, Article number: 6529 (2015)
7	Mol_Wt	Molecular weight based on rule of mixtures	n/a
8	VEC	Valence electron concentration	JOM, Vol. 66, No. 10, 2014, 2009-2020
9	VECD	Valence electron concentration difference, calculated similar to ASD	n/a
12	dH_Miedema	Enthalpy of mixing based on binary, equi-atomic, Miedema enthalpy terms	Materials Chemistry and Physics, 132 (2012) 233-238
13	Omega	Disordered solid solution thermodynamic prediction parameter, Ω	Materials Chemistry and Physics, 132 (2012) 233-238
15	Singh	Disordered solid solution geometric prediction parameter, Λ	Intermetallics, 53 (2014) 112-119
16	dS_excess_div_ideal	Excess configurational entropy divided by ideal configurational entropy	Intermetallics, 59 (2015) 750-80
17	e_over_a	Itinerant electron concentration	Acta Materialia, 75 (2014) 297–306
18	Eps_Sd	e_over_a minus 1.5	Acta Materialia, 75 (2014) 297–306
19	VEC_div_CN12_AtRad	VEC divided by average atomic radius (CN12 At. R.) based on rule of mixtures	n/a
20	VEC_div_Guo_AtRad	VEC divided by average atomic radius (GUO At. R.) based on rule of mixtures	n/a
21	dH_IM_div_Mied	Enthalpy for intermetallic compound formation divided by dH_Miedema	Journal of Alloys and Compounds, 658 (2016) 603-607
22	Kappa_CR1	Disordered solid solution thermodynamic prediction parameter	Journal of Alloys and Compounds, 658 (2016) 603-607
23	Kappa_CR1_div_dH_IM_div_Mied	Kappa_CR1 divided by dH_IM_div_Mied	Journal of Alloys and Compounds, 658 (2016) 603-607
24	N_Elements	Number of elements in alloy	n/a
10	ASD_GUO	Atomic size difference based on GUO At. R.	Materials Chemistry and Physics, 132 (2012) 233-238
25	ASD_CN12	Atomic size difference based on CN12 At. R.	Materials Chemistry and Physics, 132 (2012) 233-238
26	ASD_Wiki	Atomic size difference based on Wiki-E. At. R.	Materials Chemistry and Physics, 132 (2012) 233-238
27	ASD_MEH	Atomic size difference based on MEH At. R.	Materials Chemistry and Physics, 132 (2012) 233-238
28	ASD_Zhang	Atomic size difference based on Zhang At. R.	Materials Chemistry and Physics, 132 (2012) 233-238
29	ISD_MEH	Ionic size difference based on MEH Ion. R., calculated similar to atomic size difference	Materials Chemistry and Physics, 132 (2012) 233-238
14	gamma_Guo	Effective atomic size parameter based on GUO At. R.	Scripta Materialia, 94 (2015) 28–31
30	gamma_CN12	Effective atomic size parameter based on CN12 At. R.	Scripta Materialia, 94 (2015) 28–31
31	gamma_Zhang	Effective atomic size parameter based on Zhang At. R.	Scripta Materialia, 94 (2015) 28–31
32	gamma_Wiki	Effective atomic size parameter based on Wiki-E. At. R.	Scripta Materialia, 94 (2015) 28–31
11	END_Pauling	Electronegativity difference based on Pauling scale	Materials Chemistry and Physics, 132 (2012) 233-238
33	END_Allen	Electronegativity difference based on Allen scale	Materials Chemistry and Physics, 132 (2012) 233-238
34	END_AR	Electronegativity difference based on Allred-Rochow scale	Materials Chemistry and Physics, 132 (2012) 233-238
41	dS_ideal	Ideal configurational entroy	Materials Chemistry and Physics, 132 (2012) 233-238
42	dS_excess	Excess configurational entroy	Intermetallics, 59 (2015) 750-80
48	dH_chemical	Chemical enthalpy contribution	Intermetallics, 23 (2012) 148-157
49	dH_elastic	Elastic enthalpy contribution	Intermetallics, 23 (2012) 148-157
87	dG_M_I_1200	Simple Gibbs-free model based on dH_Miedema and dS_ideal at 1200K	Materials Chemistry and Physics, 132 (2012) 233-238

Table 6. Main parameters (50 out of 91) calculated for each LDHEA composition as used for phenomenological selection rules, machine learning, and the simple phase diagram model.

3.2.4 Alloy composition range

The main focus of the LDHEA design has been on 4-element and 5-element alloys based on 19 elements of the periodic table in a composition range per element of 5at.-% to 45at.-% and restricting compositions of interest by calculated raw LDHEA metal price (<5$/kg) and LDHEA mass density (<5g/cc). Subsequent filtering was performed by phenomenological means, including CALPHAD, or a simple phase diagram model.

However, to get a better understanding of the alloy design in the LDHEA space, alloys ranging from 2 to 8 elements have been evaluated. Similarly, the composition range per element in an initial stage was kept broader ranging from 5at.-% to 90at.-%. Compositional resolution varies (2at.-% to 15at.-%) dependent on number of elements in an alloy (from 2 to 8), and how many elements of the periodic table are being considered (from 16 to 33) to limit computation time. See Table 7 for some examples.

Computation time can vary from less than an hour to a few days per batch. These computations are described in the section "Computations for high-throughput material design".

ID	Elements in LDHEA	Elements from Periodic table	Elements selected from Periodic Table	Range	Resolution
1	4	16	B, Mg, Al, Si, Ti, V, Cr, Mn, Fe, Co, Ni, Zr, Nb, Mo, Ta, W	5-85at.-%	10at.-%
2	4	21	Li, Be, B, Mg, Al, Si, Ti, V, Cr, Mn, Fe, Co, Ni, Cu, Zn, Y, Zr, Nb, Mo, Ta, W	5-85at.-%	10at.-%
3	4	26	Li, Be, B, Mg, Al, Si, Ti, V, Cr, Mn, Fe, Co, Ni, Cu, Zn, Y, Zr, Nb, Mo, Sn, Sb, Ta, W, Bi, Ce, Gd	5-85at.-%	10at.-%
4	4	31	Li, Be, B, Mg, Al, Si, Ti, V, Cr, Mn, Fe, Co, Ni, Cu, Zn, Ga, Ge, Y, Zr, Nb, Mo, Cd, Sn, Sb, Hf, Ta, W, Pb, Bi, Ce, Gd	5-85at.-%	10at.-%
5	3	19	Li, B, Mg, Al, Si, Ti, V, Cr, Mn, Fe, Co, Ni, Cu, Zn, Zr, Nb, Mo, Ta, W	5-90at.-%	5at.-%
6	4	19	Li, B, Mg, Al, Si, Ti, V, Cr, Mn, Fe, Co, Ni, Cu, Zn, Zr, Nb, Mo, Ta, W	5-85at.-%	5at.-%
7	5	19	Li, B, Mg, Al, Si, Ti, V, Cr, Mn, Fe, Co, Ni, Cu, Zn, Zr, Nb, Mo, Ta, W	5-80at.-%	5at.-%
8	6	19	Li, B, Mg, Al, Si, Ti, V, Cr, Mn, Fe, Co, Ni, Cu, Zn, Zr, Nb, Mo, Ta, W	5-75at.-%	5at.-%
9	3	16	Li, Mg, Al, Si, Ti, V, Cr, Mn, Fe, Co, Ni, Cu, Zn, Mo, Y, Zr	10-60at.-%	2at.-%
10	4	16	Li, Mg, Al, Si, Ti, V, Cr, Mn, Fe, Co, Ni, Cu, Zn, Mo, Y, Zr	5-45at.-%	2at.-%
11	5	16	Li, Mg, Al, Si, Ti, V, Cr, Mn, Fe, Co, Ni, Cu, Zn, Mo, Y, Zr	5-35at.-%	2at.-%
12	6	16	Li, Mg, Al, Si, Ti, V, Cr, Mn, Fe, Co, Ni, Cu, Zn, Mo, Y, Zr	5-35at.-%	2at.-%
13	3	28	Li, B, Na, Mg, Al, Si, K, Ca, Sc, Ti, V, Cr, Mn, Fe, Co, Ni, Cu, Zn, Y, Zr, Mo, Sn, Sb, Ba, Ce, Ta, W, Bi	Equiatomic	n/a
14	4	28	Li, B, Na, Mg, Al, Si, K, Ca, Sc, Ti, V, Cr, Mn, Fe, Co, Ni, Cu, Zn, Y, Zr, Mo, Sn, Sb, Ba, Ce, Ta, W, Bi	Equiatomic	n/a
15	5	28	Li, B, Na, Mg, Al, Si, K, Ca, Sc, Ti, V, Cr, Mn, Fe, Co, Ni, Cu, Zn, Y, Zr, Mo, Sn, Sb, Ba, Ce, Ta, W, Bi	Equiatomic	n/a
16	6	28	Li, B, Na, Mg, Al, Si, K, Ca, Sc, Ti, V, Cr, Mn, Fe, Co, Ni, Cu, Zn, Y, Zr, Mo, Sn, Sb, Ba, Ce, Ta, W, Bi	Equiatomic	n/a
17	7	28	Li, B, Na, Mg, Al, Si, K, Ca, Sc, Ti, V, Cr, Mn, Fe, Co, Ni, Cu, Zn, Y, Zr, Mo, Sn, Sb, Ba, Ce, Ta, W, Bi	Equiatomic	n/a
18	8	28	Li, B, Na, Mg, Al, Si, K, Ca, Sc, Ti, V, Cr, Mn, Fe, Co, Ni, Cu, Zn, Y, Zr, Mo, Sn, Sb, Ba, Ce, Ta, W, Bi	Equiatomic	n/a

Table 7. Examples of LDHEA design criteria related to elements of the periodic table, composition range per element, and composition resolution within composition range for LDHEA.

3.3 High-throughput experimentation

3.3.1 Combinatorial, sputtered, thin-film, compositional gradients

Intermolecular's high-throughput, combinatorial, thin-film, sputter platform was used for mapping the composition space within each alloy of interest. Films were deposited by co-sputtering from up to 5 sputter guns to deposit up to 5 elements simultaneously. Compositional gradients of 100mm x 100mm with a thickness ranging from 100-250nm for basic characterization to >1,000nm for nano-indentation were deposited onto thermally-oxidized silicon wafers.

Annealing of the compositional gradient films was performed for 10-60min under inert/reducing atmosphere. Anneal temperatures were selected either based on CALPHAD or rule of mixtures. Characterization and nano-indentation is mainly performed after annealing.

The compositional gradient films were analyzed by X-ray diffraction, and tested for hardness by nano-indentation. Composition was monitored by Energy Dispersive X-ray Spectroscopy (EDS), and X-ray Fluorescence (XRF), calibrated by Rutherford Back Scattering (RBS). This way, maps of composition (e.g. XRF), phases (e.g. XRD), and hardness (nano-indentation) can be created per compositional gradient (100mm x 100mm) coupon, typically with a grid of 5, 16, or 25 points per coupon. Multiple coupons are required to map the complete composition space (see Figure 2), yet most work was performed away from phase diagram corners and edges.

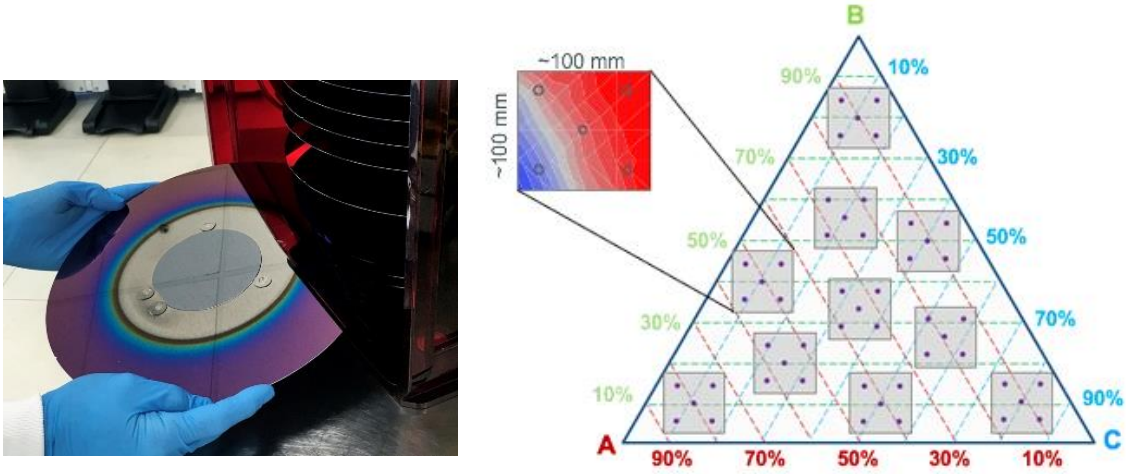

Figure 2. Sputtered, thin-film, compositional gradient (left), and example of distribution of coupons to map a ternary phase diagram (right).

3.3.2 Bulk samples

Bulk samples were manufactured by ball milling (mechanical alloying), arc, or induction melting. Powder consolidation (hot isostatic pressing, or HIP) was used to convert the ball-milled powders into cylinders for mechanical testing.

Most ball milling was performed at room temperature for either 5 gram or 200 gram batch size, starting from -325mesh, 3N-purity atomized powders with a small amount of organic added to minimize cold welding. Most powders were elements, except for the use of Li50Al50, and Mn50Fe50 alloy powders. Arc and induction melting were used to manufacture 3N-purity bulk samples, typically either 0.75”-diameter by 0.25”-thick pucks for basic characterization, or 0.5”-diameter by 0.75”-high cylinders for compressive or tensile stress-strain tests.

Annealing of the 5 gram batches of ball-milled powder was performed for 1 hour under Ar-2%H2 atmosphere with positive pressure up to 4-5 psi. Cooling was conducted to room temperature with average cooling rate of 3-5 °C/s. Arc and induction melted pucks were annealed for 18hrs. Anneal temperatures were selected either based on CALPHAD or rule of mixtures. Characterization and mechanical testing is mainly performed after annealing, except for ball milling, where powders are characterized prior to and after annealing.

Bulk samples were analyzed by X-ray diffraction, and tested for Vickers hardness. Photos were taken on individual indents to investigate pile up as an indication for ductility (malleability). Composition was monitored by Energy Dispersive X-ray Spectroscopy (EDS), and Inductively Coupled Plasma Optical

Emission Spectrometry (ICP-OES). Toughness, and malleability were qualitatively monitored by both hammering pucks and drilling holes in pucks with carbide bits. Quantitative mechanical testing was performed by both compressive and tensile stress-strain setups.

4 Project activities and accomplishments

4.1 High-throughput material design

4.1.1 Statistical analysis of phenomenological parameters for experimental HEA database

As shown in Table 8, the electronegativity difference based on the Allred-Rochow scale (END_AR) ranks as the most significant phenomenological parameter for single-phase, disordered, solid solutions (SPSS) for the experimental HEA database, followed by a few other electronegativity parameters (not shown). Subsequently, the atomic size difference, based on coordination number equal to 12 (ASD_CN12), ranks as the second most significant (non-electronegativity) parameter.

Both END_AR and ASD_CN12 are more significant than any of the thermodynamic parameters. The significance (p-value) of these two parameters is much higher than the significance of more recent parameters like “Singh”, or “Omega”, yet 80% of the investigated parameters are considered significant (p-value < 0.05).

The analysis suggests a larger probability of SPSS for higher mass density (positive p-value), which is not in favor of LDHEA. In addition, a larger probability of SPSS for alloys is expected with fewer elements (negative p-value).

The importance of the electronegativity difference for LDHEA has been addressed recently in literature (5). The weaker significance of “Omega” has been discussed (11, 16). Furthermore, it is known that cut-off values of these parameters are often considered “necessary, but not sufficient” in guiding SPSS HEA design.

ID	Parameter	p-value	t-statistic	Comments
		<5.E-02		Considered Significant
1	END_AR	8.E-36	-14.3	END based on Allred-Rochow scale
6	ASD_CN12	1.E-25	-11.5	ASD based on coordination number 12
10	dS_excess	5.E-22	10.2	Excess Configurational Entropy
11	gamma_CN12	8.E-22	-10.2	Effective atomic size parameter
12	dS_excess_div_ideal	2.E-20	9.7	Excess divided by ideal entropy
15	dH_elastic	4.E-15	-8.1	Elastic Enthalpy
18	VECD	1.E-13	-8.0	VEC difference
20	dG_M_I_1200	3.E-12	7.4	Simple Gibbs-free energy @ 1200K
22	Density	1.E-11	7.2	Mass Density
26	dH_miedema	7.E-11	6.8	Enthalpy of mixing based on Miedema
35	N_Elements	2.E-08	-5.9	Number of elements
46	Youngs_Modulus	7.E-07	5.1	Young's Modulus
50	dS_ideal	4.E-06	-4.7	Ideal configurational entropy
58	Singh	1.E-05	4.5	Geometric Singh parameter
67	VEC	2.E-04	3.9	Valence Electron Concentration
72	Omega	2.E-02	2.4	Thermodynamic Omega parameter
75	Eps_Sd	8.E-02	-1.8	e_over_a minus 1.5
76	e_over_a	8.E-02	-1.8	Itinerant electron concentration
77	Kappa_CR1_div_dH_IM_div_Mied	2.E-01	-1.3	Thermodynamic parameter
80	Price	3.E-01	1.2	Price
87	Kappa_CR1	7.E-01	0.4	Thermodynamic parameter

Table 8. Statistical analysis based on the experimental HEA database for the 91 parameters shows that the electronegativity difference and atom size difference are most significant for single-phase disordered solid solution (SPSS).

4.1.2 Phenomenological selection rules and machine learning

When relying on visual cut-off values in graphs, as often done in literature, trends can be recognized for the location of the largest population of SPSS. Graphs of ASD_CN12 vs END_Pauling, ASD_CN12 vs Omega, and ASD_CN12 vs gamma_CN12 for the experimental HEA database show that most SPSS are captured by ASD_CN12 < 7%, END_Pauling < 0.20, Omega > 1.1, and gamma_CN12 < 1.175, with similar values often used in literature.

Figure 3 shows the reduction in number of alloy compositions for 2 to 6 element LDHEA based on 28 elements of the periodic table when introducing a phenomenological filter combined with both a density and price filter. Less than 10 compositions are left from the initial 100,000's of possibilities as potential equi-atomic SPSS LDHEA based on this filter. Less than 5,000 compositions are left from the initial 100's of millions of off-equi-atomic possibilities. As previously mentioned, these phenomenological selection rules (cut-off values) are considered necessary, not sufficient, which means that the actual number of SPSS LDHEA candidates is likely smaller.

Finally, when considering more strict phenomenological selection rules for LDHEA, e.g. ASD_Guo < 4.5%, END_Pauling < 0.175, and Omega > 10 (5) for 23 common elements in 5-element LDHEA in a range of 5-45at.-% and step size of 5at.-%, the number of potential candidates gets further reduced drastically with only a handful of candidates, see Table 9. These are Al-Zn-based alloys. These alloys combine easy boilers (Li, Mg, Zn) with high melters (Cr, Cu, Fe).

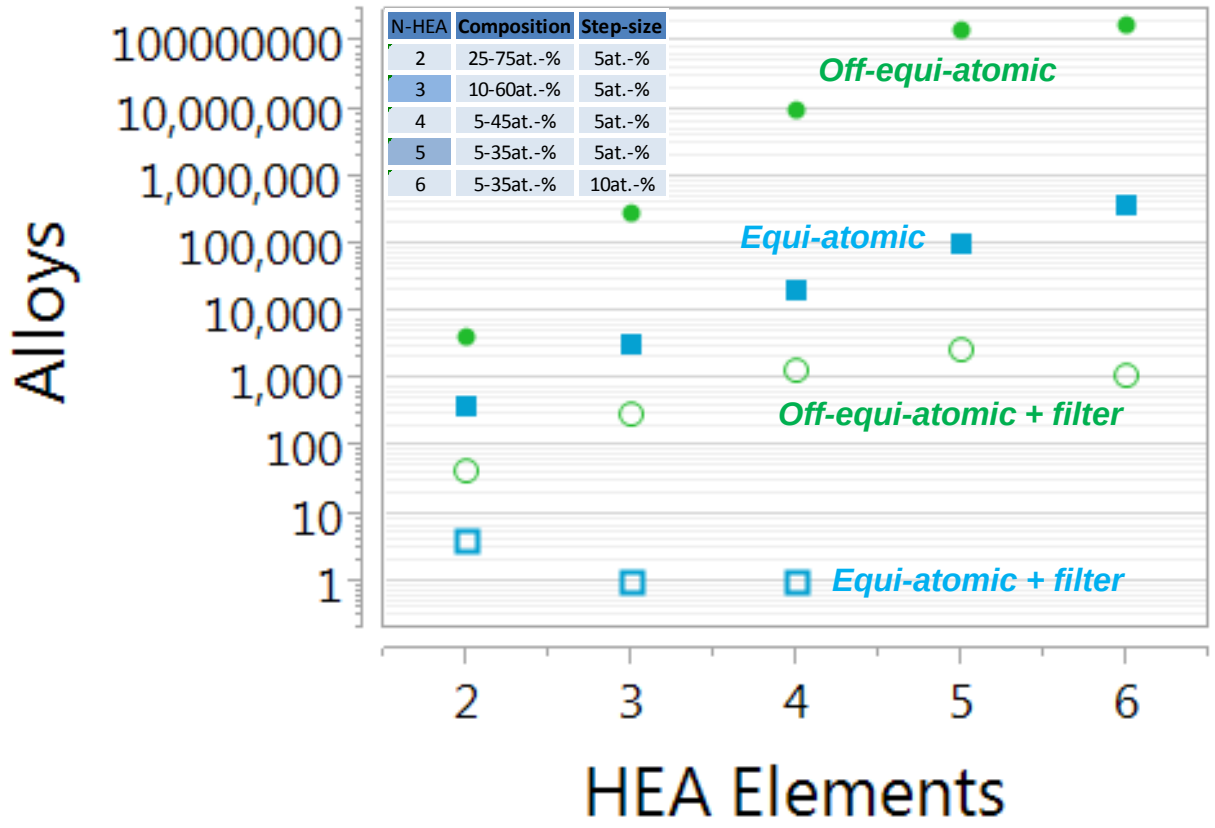

Figure 3. Number of alloy compositions versus number of elements in the HEA when considering 28 elements of the periodic table for both equi-atomic and off-equi-atomic compositions, both with and without an HEA design filter. The applied filter is the following: END_Pauling < 0.20, ASD_CN12 < 7%, Omega > 1.1, gamma_CN12 < 1.175, Density < 5g/cc, and Price < 5$/kg.

e1	e2	e3	e4	e5	pc1	pc2	pc3	pc4	pc5	N_Elements	Price	Density	ASD_GUO	END_Pauling	Omega
Li	Mg	Al	Cr	Zn	5	5	45	5	40	5	3.6	4.3	4.4	0.156	14
Li	Mg	Al	Cr	Zn	5	5	40	5	45	5	3.5	4.5	4.4	0.157	17
Li	Mg	Al	Cu	Zn	5	5	45	5	40	5	3.3	4.4	4.1	0.170	10
Li	Al	Cr	Cu	Zn	5	45	5	5	40	5	3.7	4.7	3.9	0.158	30
Li	Al	Cr	Cu	Zn	5	45	5	10	35	5	3.9	4.7	4.4	0.170	30
Li	Al	Cr	Cu	Zn	5	40	5	5	45	5	3.6	4.9	3.9	0.158	58
Li	Al	Cr	Cu	Zn	5	40	5	10	40	5	3.8	4.9	4.4	0.170	64
Li	Al	Fe	Cu	Zn	5	45	5	5	40	5	3.2	4.7	4.0	0.164	16
Li	Al	Fe	Cu	Zn	5	40	5	5	45	5	3.1	4.9	4.0	0.165	21
Li	Al	Cr	Fe	Zn	5	45	5	5	40	5	3.4	4.6	4.3	0.152	12
Li	Al	Cr	Fe	Zn	5	40	5	5	45	5	3.4	4.8	4.2	0.152	18

Table 9. Potential 5-element SPSS LDHEA candidates when filtering for ASD_Guo < 4.5%, END_Pauling < 0.175, Omega > 10, Density <5g/cc, and Price < 5$/kg for 23 elements of the periodic table in range of 5-45at.-% in steps of 5at.-%. e1 = element 1, pc1 = at.-% e1. See Table 6 for other column headers.

In an attempt to improve on the visual cutoffs based on a handful of phenomenological parameters, machine learning was introduced based on 91 parameters and the experimental HEA database to guide

SPSS LDHEA design. The main method for the machine learning was Recursive Partitioning, a method that constructs decision trees to classify data based on a set of input and output variables (also referred to as Classification and Regression Trees, CART). The trained model provides a confidence level whether a composition will exist as an SPSS. Applying this to billions of compositions combined with mass density and price filters reduces the number of compositions to only a few thousand, see Figure 4.

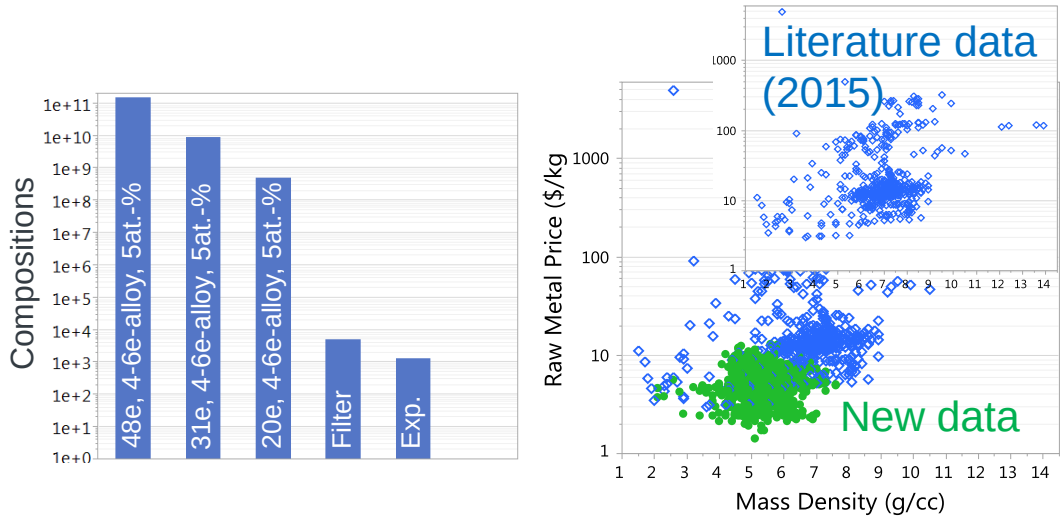

Figure 4. Left: Number of alloy compositions for sum of 4-element, 5-element-, and 6-element alloys based on 5at.-% steps per element for SPSS LDHEA design, for 48 (48e), 31 (31e), and 20 (20e) common elements of the periodic table. Filtering (Filter) based on a trained machine learning model for a confidence level >0.50, and both density <5g/cc and price <5$/kg reduces the potential SPSS LDHEA candidates from 150 billion to a few thousand. The number of experimental compositions (Exp.) evaluated in this project is of the same order of magnitude. Right: Overview of new experimental LDHEA data points generated during this project plotted versus calculated raw alloy price and mass density.

A distribution plot of the confidence level for the existence of SPSS for quarternary LDHEA with each element in a range of 5-85at.-% in steps of 10at.-% and starting from 31 common elements of the periodic table is shown in Figure 5 (left graph). Roughly 3% of the population, without filtering for mass density and price, shows a confidence level >0.50. When filtering for mass density (<5g/cc), price (<5$/kg), confidence level (>0.50), and reducing the composition range per element from 5-85at.-% to 5-45at.-% only about 350 compositions are left from the initial 2 million compositions, see Figure 5 (right graph).

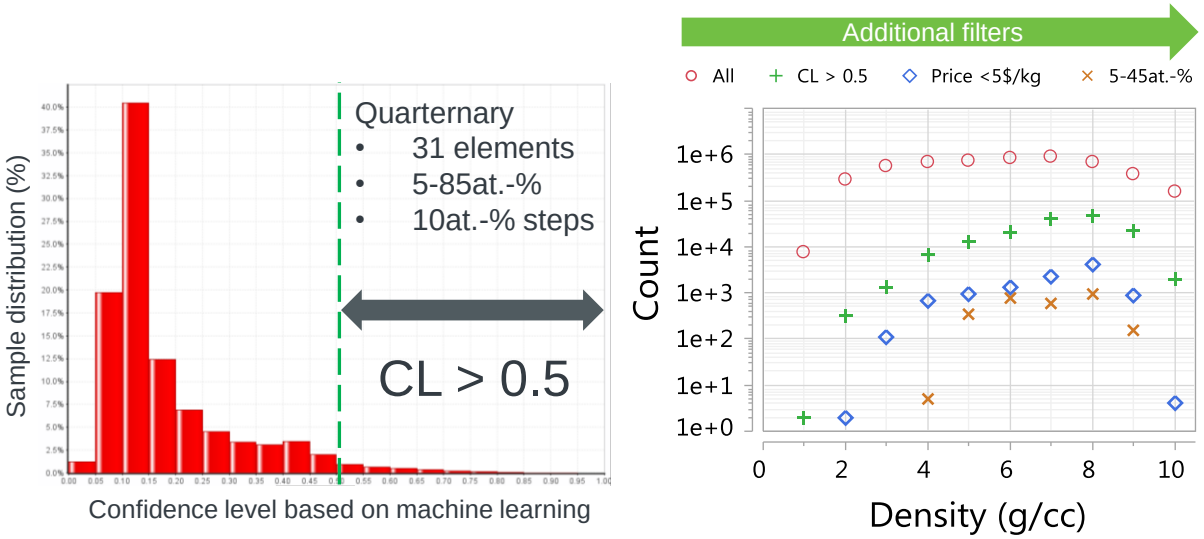

Figure 5. Left: Distribution plot of the confidence level for the existence of SPSS for 4-element LDHEA starting from 31 common elements in a range of 5-85at.-% in steps of 10at.-%. Right: Population of 4-element LDHEA when progressively adding more filters. All = 5-85at.-%, 10at.-% steps, 31 common elements, 4-element LDHEA. Subsequently, additional filters (CL > 0.5, Price < 5$/kg, range 5-45at.-%) are being added.

As a result of these material design efforts, combined with initial experimental results showing only hard, brittle, BCC, SPSS LDHEA, the constraints were slightly relaxed for mass density, and price, now including mass densities slightly over 5g/cc, and prices slightly over 5$/kg. In addition, since there is no strong argument to only pursue SPSS LDHEA (11, 17), multinary-phase LDHEA containing 2 (or more) phases were pursued as well, provided that the majority phase is a simple, disordered, solid solution (e.g. FCC) to guarantee a reasonable level of ductility.

4.1.3 Simple phase diagram (SPD) model

Both phenomenological selection rules and CALPHAD are very powerful alloy design tools. However, they also have their weaknesses, see Table 2. Therefore, a 3rd tool has been developed to allow for temperature-aware, phase diagram construction for experimentally unassessed systems. This new tool, simple phase diagrams (SPD), allows for the calculation of a simple phase diagram by constructing the Gibbs-free energy convex hull.

Formation enthalpies for ordered compounds are based on DFT calculations (https://materialsproject.org/) without entropy terms. Only fully ordered compounds are being considered, no ordered compounds with fractional occupancies are included. Disordered solid solutions are modeled based on either binary equi-atomic Miedema enthalpy terms (3), or the sum of chemical and elastic enthalpy terms (12) with either ideal or the sum of ideal and excess configurational entropy (13) terms.

Table 10 shows a steady increase from 0.68 to 0.81 in accuracy of the prediction of SPSS for a large experimental HEA database going from the simplest model for disordered solid solutions to the most advanced disordered solid solution model considered in this project.

The simplest model relies on binary equi-atomic Miedema enthalpies and the ideal configurational entropy only. These are the most typical terms considered in literature in design of HEA. The most advanced model relies on the sum of binary chemical and elastic enthalpy terms with the sum of the ideal and excess configurational entropy. It should be noted that accuracy increased significantly by lowering the temperature below what would be considered a typical anneal temperature (e.g. 85% of melting temperature). Temperatures were 43% of melting temperature based on rule of mixtures, or 35% of (melting) transition temperature based on CALPHAD when system fully assessed in CALPHAD. Furthermore, the high accuracy might be due to the concentration of experimental literature data around more ideally behaving HEA (11).

	Model		TP	FP	FN	TN	ACC
	ΔH	ΔS					
SPSS	M	I	43	103	59	294	0.68
	M	IE	41	89	61	308	0.70
	CE	I	35	32	67	365	0.80
	CE	IE	35	30	67	367	0.81

Table 10. Accuracy (ACC) predicting SPSS for different simple phase diagram models. ΔH = enthalpy. ΔS = entropy. M = equi-atomic Miedema enthalpy terms. CE = sum of chemical and elastic enthalpy terms. I = ideal configurational entropy. IE = sum of ideal and excess configurational entropy. TP = true positive. FP = false positive. FN = false negative. TN = true negative.

4.1.4 CALPHAD

CALPHAD was used to investigate the SPSS LDHEA design results from phenomenological selection rules, machine learning, simple phase diagrams, or used as a source for SPSS LDHEA design itself. However, CALPHAD was the main source of LDHEA design in the pursuit of multi-phase LDHEA with the majority phase being a simple disordered solid solution (e.g. FCC).

The automated search within CALPHAD for multi-phase LDHEA was filtered for fraction of binary phase diagrams assessed in the CALPHAD database (16) being equal to 1.0 (all binaries assessed), FCC volume fraction >0.70, number of phases 2-3, mass density (<5g/cc), and price (<5$/kg). The most likely candidates based on CALPHAD were multi-phase LDHEA based on Ca-Mn-Fe, e.g. Ca-Mn-Fe-Ni, Ca-Mn-Fe-La, Si-Ca-Mn-Fe, or Al-Zn-based alloys, e.g. Al-Mn-Cu-Zn, and Al-Si-Cu-Zn. Other automated searches, where the number of assessed binaries and volume fraction of FCC was monitored, yet with slightly

relaxed filters, resulted in Mg-Mn-Fe-Co, and Li-Mg-Mn-Fe as potential multinary LDHEA candidates. These candidates combine easy boilers (Li, Mg) with high melters (Mn, Fe, Co).

CALPHAD was compared to experimental results achieved during the project, see Figure 6. Typically, comparison of XRD results with CALPHAD results showed limited overlap. There can be multiple reasons for the discrepancies. First of all, experimental results are not necessarily fully equilibrated, where CALPHAD results assume full equilibrium. Secondly, CALPHAD historically has been designed to be accurate in the corners of phase diagrams, not around equi-atomic compositions for multinary alloys. Furthermore, often not all binary and ternary phase diagrams are assessed in CALPHAD, necessary to improve accuracy in the region around equi-atomic compositions for quarternary and quinary alloys. Finally, experimental results might include errors.

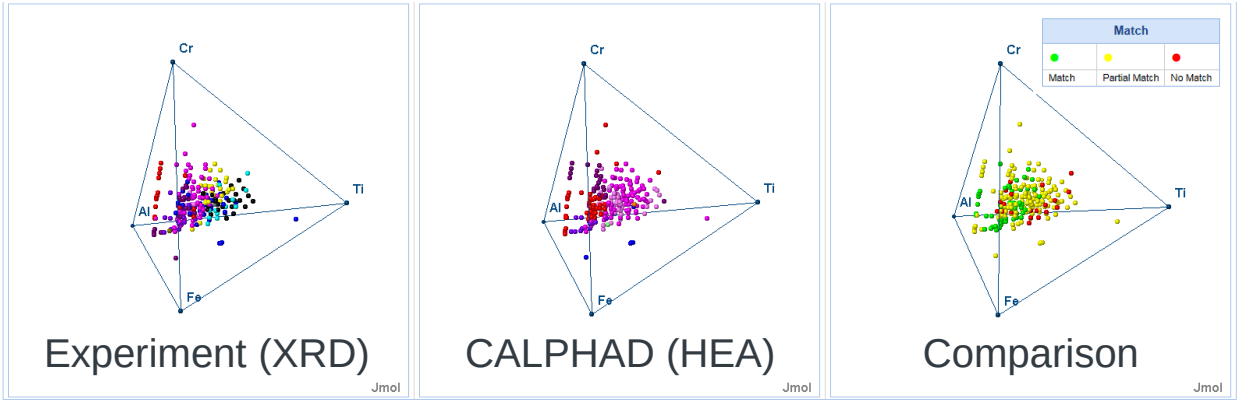

Figure 6. Isothermal phase diagram for Al-Ti-Cr-Fe based on XRD on annealed, thin films (left) and CALPHAD (middle). Different colors represent different phase space. The right tetrahedron shows the comparison of the XRD and CALPHAD results.

4.1.5 Comparison SPSS accuracy for different design methods

When comparing the accuracy of machine learning, CALPHAD, and simple phase diagrams (SPD), the database used to train the machine learning model cannot be used, since this would bias the results of machine learning. Therefore, machine learning was trained on a smaller database, and all 3 methods were compared based on another database.

Machine learning shows an accuracy of 82% in identifying which compositions are SPSS HEA, see Table 11. Calculation of Phase Diagrams (CALPHAD) shows an accuracy of 71-77% for the alloys supported by the CALPHAD database, where 30% of the compiled HEA database is not supported by CALPHAD. The accuracy for single phase diagrams was 78%. Recently, phenomenological selection rules and CALPHAD predictions were compared for a handful of systems (18).

Model	TP	FN	FP	TN	Accuracy
Machine Learning	0.33	0.02	0.16	0.49	0.82
Simple Phase Diagrams	0.31	0.04	0.18	0.47	0.78
CALPHAD-DB1	0.20	0.10	0.13	0.57	0.77
CALPHAD-DB2	0.21	0.10	0.19	0.50	0.71

Table 11. Accuracy predicting SPSS for machine learning, simple phase diagrams (SPD), and two different CALPHAD databases. TP = true positive. FP = false positive. FN = false negative. TN = true negative.

As mentioned previously, the high accuracy might be due to the concentration of experimental literature data around more ideally behaving HEA (11).

4.2 High-throughput experimentation

4.2.1 Combinatorial, sputtered, thin-film, compositional gradients

High-throughput experimentation allowed us to triple the existing experimental HEA database as published in the past 10 years in less than 2 years which happened at a rate 10x higher than previous methods. See Figure 4 for the population of new data expressed in mass density and alloy price.

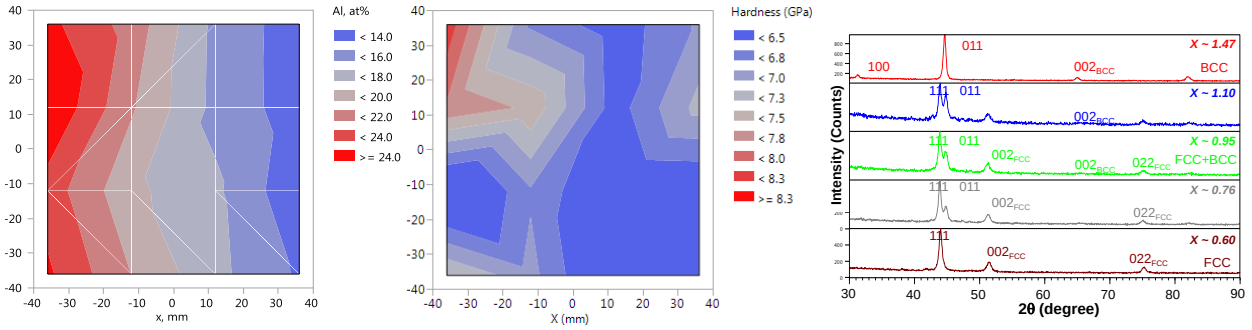

Figure 7. Left: Map of at.-% Al for $Al_xCrFeCoNi$ gradient film as measured by EDX. Middle: Hardness map for same $Al_xCrFeCoNi$ gradient film as measured by nano-indentation. Right: XRD graphs for $Al_xCrFeCoNi$ gradient film with varying x in $Al_xCrFeCoNi$. Films are annealed at 800C for 10min in inert/reducing atmosphere.

A typical example of a sputtered, thin-film, compositional gradient is shown in Figure 7. The left map shows the aluminum atomic concentration as a function of location in an $Al_xCrFeCoNi$ film with a thickness of 100nm. The accompanying nano-indentation hardness map is shown in the middle. An increase in hardness is observed with an increase in Al concentration. This might be explained by going from the softer FCC to the harder BCC with increasing Al concentration. The right graphs shows the XRD

spectra for $Al_xCrFeCoNi$ thin films with a change in Al concentration. This thin-film XRD data is in good agreement with literature data on cast samples annealed at 1100C for 24hrs (19).

We were able to show 100% agreement of crystal structures observed for 21 thin film and bulk samples that were compared with XRD, which includes $Al_xCrFeCoNi$ (see Figure 8), a common literature example (19), and other 3-element, 4-element, and 5-element alloys. It should be noted that attempts are made to anneal sputtered, thin-film samples and bulk samples under similar conditions. This means similar soak temperatures, yet not similar soak times or ramp and cooldown rates. This is largely dictated by the need for homogenization for bulk samples requiring longer soak times (typically 18hrs), and the more reactive nature (surface area) of the thin films requiring shorter soak times (typically 10-60min). Care needs to be taken to prevent reaction with the substrate and oxygen incorporation due to air exposure, especially, for anneals at high temperatures (>500C), or reactive elements (e.g. Ti, Mg, Cu, Fe). Therefore, it is recommended to include a diffusion barrier layer and anneal films prior to breaking vacuum.

Summarizing, we showed that high-throughput thin-film combinatorial methods can be used to get insight in isothermal phase diagram slices provided proper care is taken to avoid film reaction.

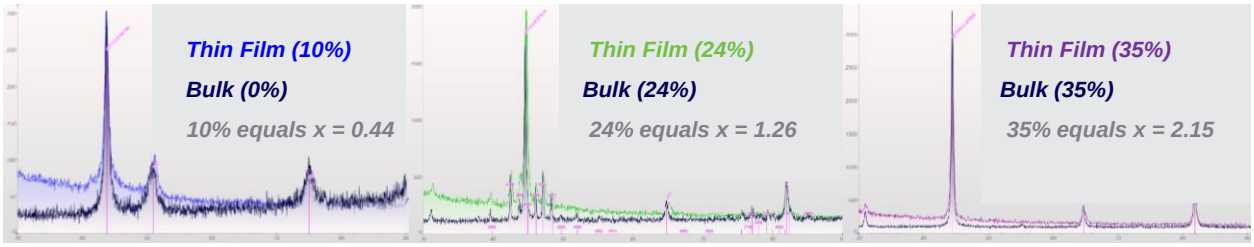

Figure 8. XRD comparison for sputtered, thin-films with ball-milled powders for $Al_xCrFeCoNi$ shows good agreement between thin-film and bulk spectra.

Although it is straightforward to map hardness as a function of composition for sputtered, thin-film, compositional gradients by nano-indentation and compare the results to micro-indentation on bulk samples, the simultaneous impact of composition, roughness, film density, and microstructure (for sufficiently thick films to avoid substrate effects) on hardness requires monitoring all these properties as a function of location on the compositional gradient, including dissecting the impact of these 4 factors on the hardness map. These additional efforts impact throughput significantly. Nevertheless, we were able to show a reasonable correlation between thin-film and bulk samples when comparing thin films to bulk literature data for pure Ti (20), pure Al (21), and AlCrFe (22), or when considering a typical Hall-Petch relation (21) for $Al_xCrFeCoNi$ for thin-film and bulk samples.

4.2.2 Bulk samples

Pursuing the LDHEA candidates from the SPSS LDHEA design efforts resulted mainly in LDHEA composed of transition metals (e.g. Cr, Mn, Fe, Ni, Cu) alloyed with Al. Most of these LDHEA did not contain high

concentrations of Li, Mg, or Zn due to the presence of high concentrations of high melters, and the elusive nature of Li-Mg-Al-Sc-Ti (see section 5). The combination of easy boilers (Li, Mg, Zn) at high concentrations with high concentrations of high melters are challenging to manufacture by arc or induction melting. As such, initial focus did not include high concentrations of Li, Mg, and/or Zn.

The high concentration of Al in these SPSS LDHEA, necessary to bring the mass density below 5.0g/cc, makes these materials hard and brittle, body-centered-cubic (BCC) alloys. These include alloys made from Al-Ti-Cr-Fe, Al-Cr-Fe-Cu, and Al-Ti-Cr-Mn-Fe. A related, yet multi-phase BCC alloy, based on Al-Cr-Fe-Ni (23), shows compressive strain >10% and specific compressive yield strength of 229 MPa x cc/g (Figure 9), yet does not show ductility in tensile tests due to cleavage, the latter observed by SEM imaging.

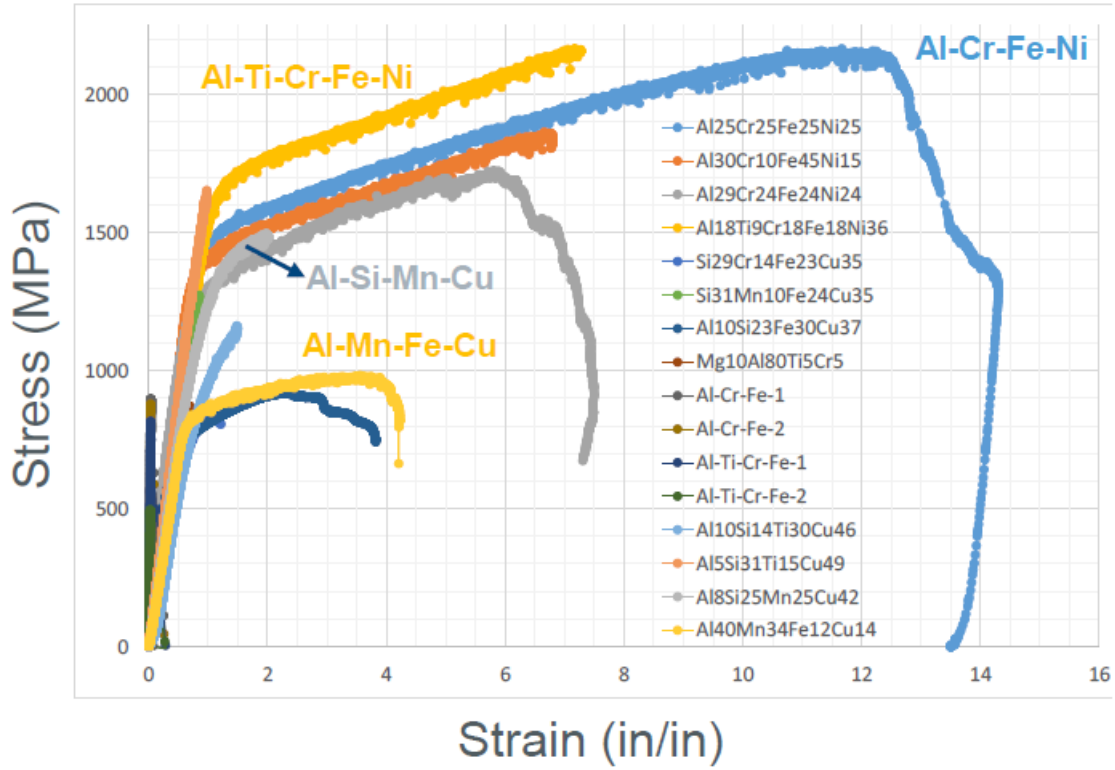

Figure 9. Compressive stress-strain curves at room temperature on 0.5”-dia x 0.75”-long cylinders manufactured by arc or induction melting followed by 18hrs anneal in inert/reducing environment.

When replacing Cr in Al-Cr-Fe-based 4- and 5-element LDHEA with Mn, hardness drops 2x, from typically 6GPa to 3GPa. Combined with compression test results, including those on the ternaries Al-Cr-Fe and Al-Mn-Fe suggest that Al-Mn-Fe-based LDHEA are still worth pursuing. Al-Mn-Fe shows compressive strain of 10-15% and specific compressive yield strength of >100 MPa x cc/g, see Figure 10. These initial results only represent one compressive stress-strain curve per composition without any property optimization. As such, reproducibility needs to be followed by optimization to show their full potential.

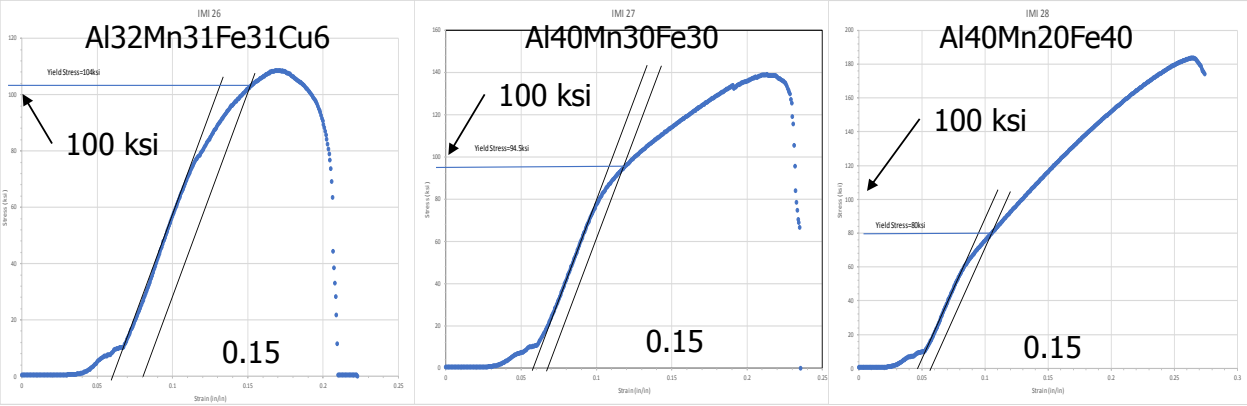

Figure 10. Compressive stress-strain curves at room temperature on 0.310"-dia x 0.775"-long cylinders manufactured by arc or induction melting followed by 18hrs anneal in inert/reducing environment.

The compressive stress-strain results on the family of Cu(Al) matrix with silicide precipitates (e.g. Al-Si-Mn-Cu, Al-Si-Fe-Cu, Al-Si-Ti-Cu) shows poor malleability (see Figure 9). Compositional mapping by EDS suggests 40-60vol.-% of silicide (Mn-Si, Fe-Si, Ti-Si) precipitates in the Cu(Al) matrix to achieve a low enough mass density.

When including Li, Mg, and Zn at high concentrations, introduced by ball milling, single-phase Li-Mg-Al-Ti-Zn LDHEA has been found with a specific ultimate compressive strength of 289MPa x cc/g, see Table 12. Al-Ti-Mn-Zn showed a specific ultimate compressive strength of 73MPa x cc/g. These initial results after hot isostatic pressing (HIP) of the ball-milled powders represent the lower end of what is possible, since no secondary processing (e.g. extrusion) has been performed to optimize strength and ductility.

ID	Formula_pc	MD (Exp)	MD (Calc)	Vicker's Hardness	H (Vickers)	CYS (=H/3)	SCYS	Ultimate Compressive Strength	UCS	SUCS
	at.-%	g/cc	g/cc		GPa	GPa	MPa cc/g	psi	GPa	MPa cc/g
1	Mg24Mn31Fe31Co14	5.7	5.5	410	4.0	1.3	237	36,906	0.3	45.0
2	Li10Mg18Al26Ti36Zn10	3.5	3.2	468	4.6	1.5	441	145,657	1.0	289.4
3	Al22Ti31Mn31Zn16	5.3	5.2	843	8.3	2.8	523	55,648	0.4	72.8
4	Li3Mg22Al3Mn26Fe46	5.4	5.1	338	3.3	1.1	203	156,148	1.1	198.3

Table 12. Mechanical test results on consolidated ball-milled powder. Consolidation by HIP. MD = Mass Density. H = Hardness in GPa. CYS = Compressive Yield Strength from Hardness. SCYS = Specific Compressive Yield Strength. UCS = Ultimate Compressive Strength from compression test. SUCS = Specific Ultimate Compressive Strength.

CALPHAD resulted in pursuit of various multinary LDHEA. Li-Mg-Al-Mn-Fe and Mg-Mn-Fe-Co ball-milled powders upon HIP show specific ultimate compressive strengths of 198MPa x cc/g and 45MPa x cc/g, respectively (Table 12). Several malleable quarternary Al-Zn-based alloys have been found upon arc/induction melting, yet with limited specific compressive yield strength (<75 MPa x cc/g). These initial results are all without any optimization for strength and/or ductility.

5 Problems encountered, departure from planned methodology, and project impact

The most significant issue we identified in the first months of the project was that neither ball-milling nor thin-film sputtering could reproduce the earlier ball-milling results reported in literature regarding $Li_{20}Mg_{10}Al_{20}Sc_{20}Ti_{30}$ LDHEA (1). Furthermore, CALPHAD was unable to reproduce the results as well, yet this might have several causes. Similarly, more strict phenomenological selection rules did not support the formation of SPSS (5), nor did machine learning.

This $Li_{20}Mg_{10}Al_{20}Sc_{20}Ti_{30}$ SPSS LDHEA system was meant both as a benchmark to validate the approach, and as a starting point for LDHEA design to replace the costly Sc with a less costly element. The work-around on the benchmarking issue was selecting a second, more well-known HEA system, $Al_xCrFeCoNi$ (19), and matching published results for that system. Regarding $Li_{20}Mg_{10}Al_{20}Sc_{20}Ti_{30}$ being a starting point for SPSS LDHEA design. The elusive nature of $Li_{20}Mg_{10}Al_{20}Sc_{20}Ti_{30}$ and the difficulty of finding promising Li-Mg-Al-based SPSS LDHEA by others (5) did raise the question whether the class of Li-Mg-Al-based SPSS LDHEA is a good starting point. As such, focus shifted towards SPSS LDHEA based on Mg, Al, and low concentrations of Si and Ti in the first year of the project.

Another issue encountered in the first year of the project was extremely low thin-film sputter deposition rates for Fe, due to its ferromagnetic properties. The issue was resolved by both redesigning the magnets of the sputter gun, and by working with binary Fe-containing sputter targets.

After meeting all the program targets of the first budget year, we encountered a major issue at the start of the second year. All LDHEA that met hardness targets in year 1 turned out to be hard and brittle (single-phase) BCC alloys showing no signs of malleability in compression testing. Therefore, a change of approach to expand alloy exploration with slightly relaxed mass density (<5.5g/cc) and price targets (<7$/kg) was proposed and implemented, including opening up the window to multinary LDHEA.

Once a multinary LDHEA was identified that showed compressive strain >10% (malleability), plans were made for a scale-up to 25lbs, provided tensile testing would show encouraging results. Unfortunately, tensile testing showed no signs of ductility, and SEM imaging showed that this was due to cleavage. Therefore, alloy exploration continued, including more use of ball milling to allow the investigation of LDHEA with volatile elements at high concentrations combined with high melting elements at high concentrations.

6 References

1. ***Koch, et al.*** *Raleigh, NC, USA : Materials Research Letters, 2015, Vol. 3. 95-99.*

2. ***Lou, A.A.*** *Warren, MI, USA : JOM, 2002, Vol. 54. 42-48.*

3. ***Yang, et al.*** *Beijing, China : Materials Chemistry and Physics, 2012, Vol. 132. 233– 238.*

4. ***Tian, et al.*** *Stockholm, Sweden : Intermetallics, 2015, Vol. 58. 1-6.*

5. ***Yang, et al.*** *Beijing, China : JOM, 2014, Vol. 66. 2009.*

6. ***Zhang, et al.*** *Madison, WI, USA : JOM, 2012, Vol. 64. 839.*

7. ***Gebhardt, et al.*** *Aachen, Germany : Thin Solid Films, 2012, Vol. 520. 5491–5499.*

8. ***Takeuchi, et al.*** *Sendai, Japan : Materials Transactions, 2005, Vol. 46. 2817-2829.*

9. ***Niessen, et al.*** *Eindhoven, The Netherlands : CALPHAD, 1983, Vol. 7. 51-70.*

10. ***Troparevsky, et al.*** *Oak Ridge, TN, USA : JOM, 2015, Vol. 67. 2350-2362.*

11. ***Miracle, et al.*** *Wright-Patterson AFB, OH, USA : Acta Materialia, 2017, Vol. 122. 448-511.*

12. ***Ghosh, et al.*** *Kalpakkam, TN, India : Intermetallics, 2012, Vol. 23. 148-157.*

13. ***Ye, et al.*** *Hong Kong, China : Intermetallics, 2015, Vol. 59. 75-80.*

14. ***King, et al.*** *Lucas Heights, NSW, Australia : Acta materialia, 2016, Vol. 104. 172-179.*

15. ***Ye, et al.*** *Hong Kong, China : Journal of Alloys and Compounds, 2016, Vol. 681. 167-174.*

16. ***Senkov, et al.*** *Wright-Patterson AFB, OH, USA : Journal of Alloys and Compounds, 2016, Vol. 658. 603-607.*

17. ***Raabe, et al.*** *Dusseldorf, Germany : JOM, 2017, Vol. 69. 2099.*

18. ***Schmid-Fetzer, et al.*** *Clausthal-Zellerfeld, Germany : J. Phase Equilib. Diffus., 2017, Vol. 38. 369–381.*

19. ***Yeh, et al.*** *Hsinchu, Taiwan : Materials Science and Engineering: B, 2009, Vol. 163. 184-189.*

20. ***Dunstan, et al.*** *London, England : Proceedings of the Royal Society A, 2016, Vol. 472. DOI: 10.1098/rspa.2015.0890.*

21. ***Armstrong, R.W.*** *College Park, MD, USA : Materials Transactions, 2014, Vol. 55. 2-12.*

22. ***Dunstan, et al.*** *London, England : International Journal of Plasticity, 2014, Vol. 53. 56-65.*

23. ***Chen, et al.*** *Xuzhou, Jiangsu, China : Materials Science & Engineering A, 2017, Vol. 681. 25-31.*